



# Rational design and preparation of nanoheterostructures based on zinc titanate for solar-driven photocatalytic conversion of CO<sub>2</sub> to valuable fuels

Jiaxue Lu, Deli Li, Yao Chai, Li Li, Meng Li, Yingying Zhang, Jun Liang\*

*State Key Laboratory of High-efficiency Utilization of Coal and Green Chemical Engineering, National Demonstration Center for Experimental Chemistry Education, College of Chemistry and Chemical Engineering, Ningxia University, Yinchuan 750021, China*



## ARTICLE INFO

### Keywords:

Zn<sub>2</sub>Ti<sub>3</sub>O<sub>8</sub>/ZnTiO<sub>3</sub>  
Zn<sub>2</sub>TiO<sub>4</sub>/R-TiO<sub>2</sub>  
Heterostructure  
Photocatalysis  
CO<sub>2</sub> reduction

## ABSTRACT

Photocatalytic reduction of CO<sub>2</sub> with H<sub>2</sub>O on photocatalysts to produce fuels presents great potential to simultaneously address energy and environmental issues. Herein, zinc titanate-based heterostructured nanohybrids including Zn<sub>2</sub>Ti<sub>3</sub>O<sub>8</sub>/ZnTiO<sub>3</sub> and Zn<sub>2</sub>TiO<sub>4</sub>/R-TiO<sub>2</sub> were designed and prepared through a two-step chemical route. When used as photocatalyst for converting CO<sub>2</sub> with H<sub>2</sub>O under UV-light irradiation, the zinc titanate-based heterostructured nanohybrids show high photocatalytic performance, with CH<sub>4</sub> and CO yields significantly higher than those obtained with Zn<sub>2</sub>Ti<sub>3</sub>O<sub>8</sub>, Zn<sub>2</sub>TiO<sub>4</sub>, and rutile TiO<sub>2</sub> as the photocatalysts. The existence of heterojunctions in the nanohybrids was demonstrated by experimental results, and electrochemical impedance spectra also reveal a favorable zinc titanate-based heterostructure. Moreover, based on theoretical calculations, the observed reduced band gap further revealed the effective light-absorption of the heterostructured nanohybrids in CO<sub>2</sub> reduction. It is thus concluded that the synergistic effect of the heterostructure promotes charge separation and fast electron transport, resulting in its enhanced photocatalytic performance in CO<sub>2</sub> reduction.

## 1. Introduction

Finding a low cost, renewable and clean energy source as an alternative to fossil fuels remains a huge challenge for researchers [1,2]. Conversion of CO<sub>2</sub> into fuels (eg. CH<sub>4</sub>, CO, CH<sub>3</sub>OH) undoubtedly presents a great potential to solve the growing energy crisis [3]. Currently, various conversion strategies have been developed to chemically reduce CO<sub>2</sub> [4]. Among them, photocatalytic CO<sub>2</sub> reduction via artificial photosynthesis is considered one of the most promising techniques for renewable fuels production. Many photocatalysts have been studied for CO<sub>2</sub> photoreduction [2,5–8], but TiO<sub>2</sub> remains the most convenient candidate considering the stability, cost, and nontoxicity [9]. However, the conversion efficiency of CO<sub>2</sub> to value added carbon products under the catalysis of TiO<sub>2</sub> is still very low due to fast electron-hole recombination.

To improve the efficiency of solar fuels production, many design strategies, including band-structure engineering, heterostructured constructing and nano-structuralization, have been proposed to develop photocatalyst materials, in which the one the most widely used is to construct photocatalyst heterojunctions [10,11]. Studies [12–14] have demonstrated that the resulting heterojunctions in those composites can remarkably suppress the recombination of electron-hole pairs and boost

the diffusion of photogenerated carriers. In recent years, titanates have been widely investigated as a potential alternative to TiO<sub>2</sub> for photocatalytic reaction due to their adjustable composition and electronic structure properties [9]. Especially, due to its excellent optical, electrical and physical chemistry properties, zinc-based titanate has been paid increasing attention [15,16]. Generally, zinc titanate exists in three different phases including ZnTiO<sub>3</sub> (hexagonal), Zn<sub>2</sub>Ti<sub>3</sub>O<sub>8</sub> (cubic), and Zn<sub>2</sub>TiO<sub>4</sub> (face-centered cubic). ZnTiO<sub>3</sub> is one of the promising materials and has been widely used for gas sensor, nonlinear optics and catalytic sorbents [17–19]. Zn<sub>2</sub>Ti<sub>3</sub>O<sub>8</sub> is a metastable form, and has received increasing attention since it exhibits suitable band-gap for photocatalytic water splitting [15]. Compared with the reported ZnTiO<sub>3</sub> and Zn<sub>2</sub>Ti<sub>3</sub>O<sub>8</sub>, cubic spinel Zn<sub>2</sub>TiO<sub>4</sub> seems to be most stable phase. When Zn<sub>2</sub>Ti<sub>3</sub>O<sub>8</sub> is heated at high temperature, it will decompose into Zn<sub>2</sub>TiO<sub>4</sub>, rutile-type TiO<sub>2</sub> and other phases [20]. Among the three different crystalline phases of zinc titanate, Zn<sub>2</sub>Ti<sub>3</sub>O<sub>8</sub> has a relatively high reducing potential [21] and is thermodynamically able to photoreduce CO<sub>2</sub> without additional reductants, and the potential of the valence band holes is much more positive than the water oxidation potential. Recent research also shows that the valence band of Zn<sub>2</sub>Ti<sub>3</sub>O<sub>8</sub> is more positive and the conduction band is more negative than the respective bands of anatase TiO<sub>2</sub> [22]. This can be conductive to the reduction of

\* Corresponding author.

E-mail address: [junliang@nxu.edu.cn](mailto:junliang@nxu.edu.cn) (J. Liang).

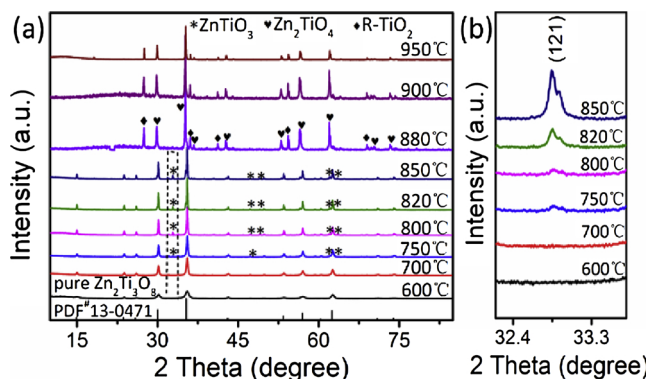


**Fig. 1.** (a) XRD patterns of products obtained at different calcination temperatures between 600°C and 950°C. (b) The enlarged part for XRD patterns of corresponding products ranging from  $2\theta = 32.1^\circ$  to  $33.8^\circ$ .

CO<sub>2</sub> driven by solar energy. Therefore, design of zinc-based titanate and their composites can be a very feasible and effective approach to achieve high-performance photocatalysts.

Herein, we developed an effective strategy to prepare zinc titanate-based composites. The strategy is a two-step chemical procedure, including hydrothermal reaction of butyl titanate with zinc acetate and high-temperature calcination under air flow. The resulting photocatalyst showed high performance in the photoconversion of CO<sub>2</sub> and water to CO and CH<sub>4</sub>. Analysis reveals that the high performance is attributed to the excellent charge separation and fast electron transport in the photocatalysts due to the formation of heterojunctions. Additionally, DFT calculations reveal that the zinc titanate-based heterostructured nanohybrids have a suitable band-gap. Reduced band gaps were observed in the zinc titanate-based heterostructured nanohybrids, implying that the heterostructured nano hybrid can increase the wavelength of absorbed light, thereby achieving high photoconversion efficiency.

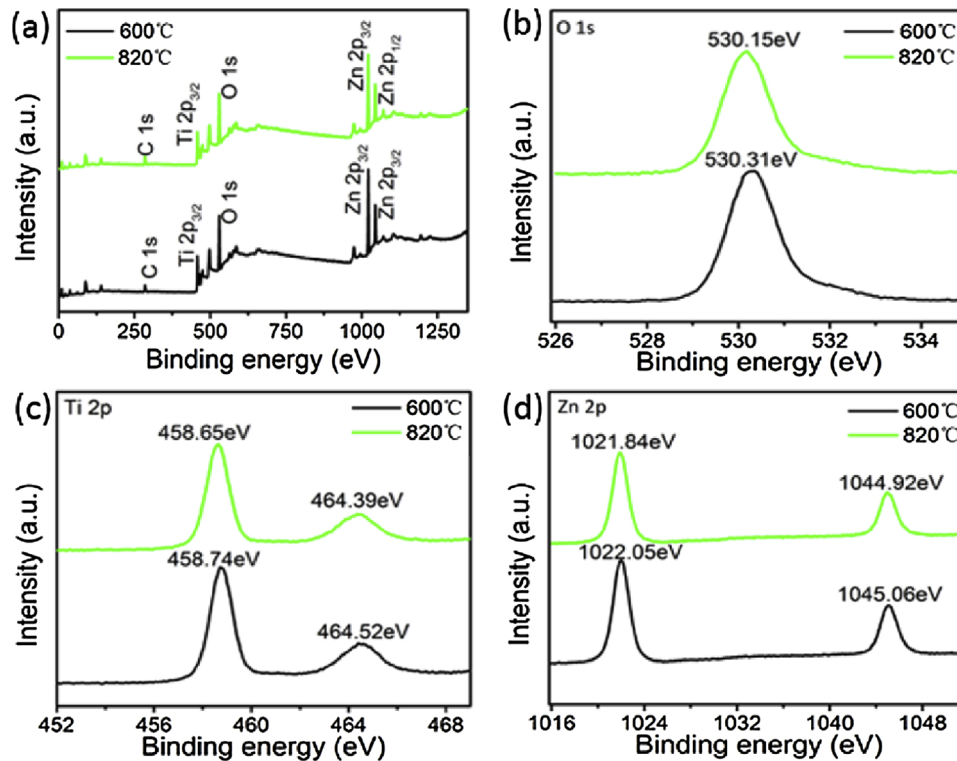


**Fig. 2.** (a) Wide scan XPS survey spectra of Zn<sub>2</sub>Ti<sub>3</sub>O<sub>8</sub> and Zn<sub>2</sub>Ti<sub>3</sub>O<sub>8</sub>/ZnTiO<sub>3</sub> (calcined at 600°C and 820°C, respectively). High resolution XPS spectra of products: (b) O 1s, (c) Ti 2p, and (d) Zn 2p of Zn<sub>2</sub>Ti<sub>3</sub>O<sub>8</sub> obtained at 600°C and Zn<sub>2</sub>Ti<sub>3</sub>O<sub>8</sub>/ZnTiO<sub>3</sub> obtained at 820 °C.

## 2. Experimental section

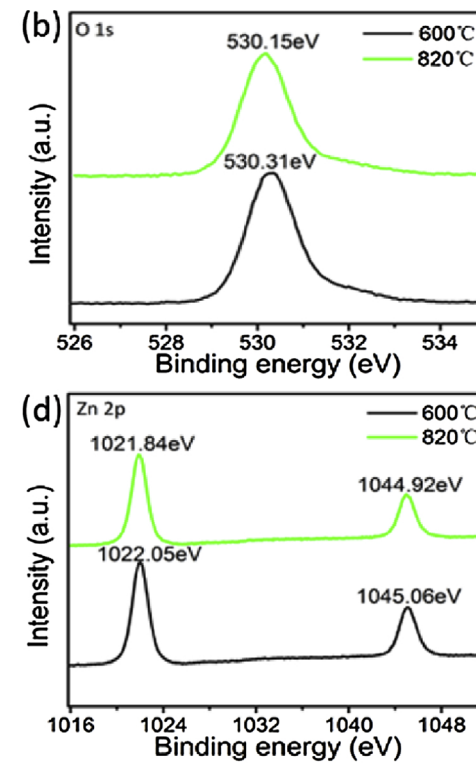
### 2.1. Catalyst preparation

Sodium titanate nanobelt (Fig. S1) was prepared by a simple modified hydrothermal route based on previous report [23]. Typical procedures of preparing the sodium titanate nanobelt are as follows: 1.5 g of NaOH was added into CH<sub>3</sub>CH<sub>2</sub>CH<sub>2</sub>OH/H<sub>2</sub>O solution (55 mL isopropyl alcohol and 10 mL deionized water) under stirring. Subsequently, 2.1 g of butyl titanate was added to the above solution and the mixture was stirred for 30 min. Then, the mixture was transferred into a 100-mL Teflon-lined stainless-steel autoclave. The autoclave was sealed and maintained at 180°C for 24 h, and then cooled to room temperature. The final products were filtered, washed with deionized water and dried at 70 °C for 12 h.

Synthesis of zinc titanate-based heterostructures: In a typical two-step process, the as-obtained sodium titanate (0.151 g) and zinc acetate (3.5 mmol) were added to 18 mL of deionized water, and the mixture was stirred for 1 h. The solution was then transferred into a 25-mL Teflon-lined stainless steel autoclave and maintained at 200°C for 24 h in an oven. After natural cooling, the product was washed repeatedly with distilled water and then dried at 70°C for 12 h. In the next step, the dried product was calcined at 600, 700, 750, 800, 820, 840, 880, 900 and 950 °C, respectively, and maintained for 3 h at each temperature. Different samples were thus obtained. For comparison, the rutile TiO<sub>2</sub> (R-TiO<sub>2</sub>) was prepared by heating commercial anatase TiO<sub>2</sub> at 950°C for 6 h. The bulk Zn<sub>2</sub>TiO<sub>4</sub> was synthesized by heating a stoichiometric mixture of TiO<sub>2</sub> and ZnO at 1200 °C for 24 h.

### 2.2. Characterization

X-ray powder diffraction (XRD) was taken on a Bruker D8 Focus power diffractometer with Cu K $\alpha$  radiation (40 kV/mA) to verify the crystal structure of obtained samples. To investigate the surface chemical composition of samples, X-ray photoelectron spectroscopy (XPS)



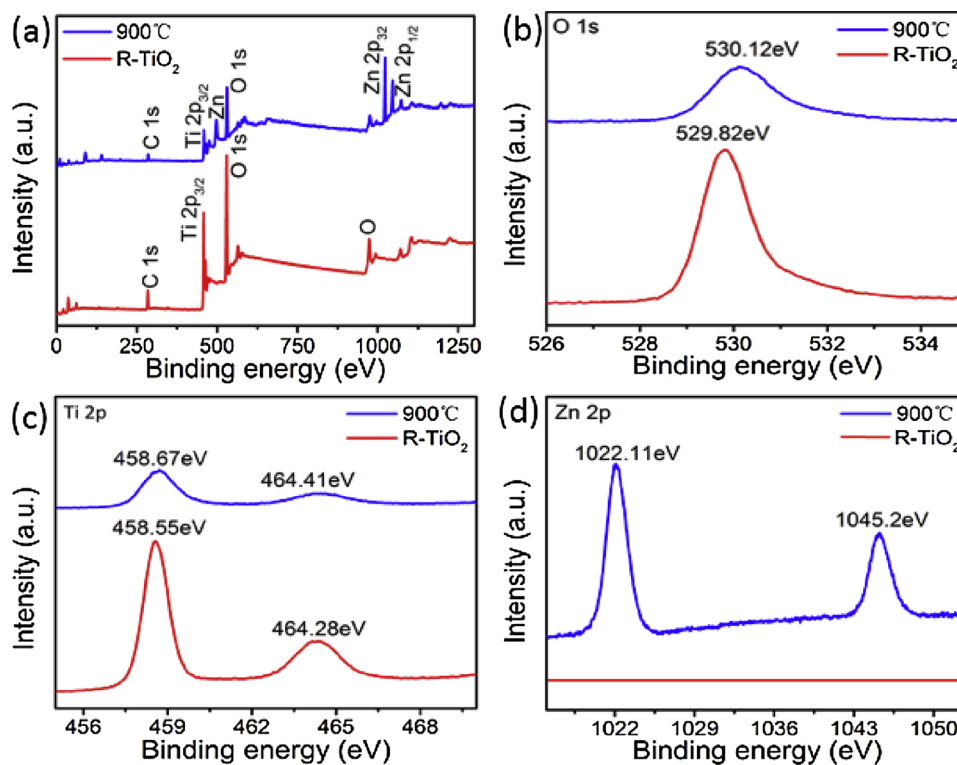


**Fig. 3.** (a) Wide scan XPS survey spectra of  $\text{Zn}_2\text{TiO}_4/\text{R-TiO}_2$  obtained at calcination temperature of  $900^\circ\text{C}$  and  $\text{R-TiO}_2$ . XPS spectra of  $\text{Zn}_2\text{TiO}_4/\text{R-TiO}_2$  obtained at  $900^\circ\text{C}$  and  $\text{R-TiO}_2$ : (b) O 1s, (c) Ti 2p, and (d) Zn 2p.

was performed on an ESCALAB 250 Xi (Thermo Fisher Scientific) electron spectrometer with Al Ka ( $\text{h}\nu = 1486.6 \text{ eV}$ ). The diffuse reflectance spectra of samples during a range from 200 to 800 nm were recorded using a Varian Cary 500 Scan UV/Vis system. In addition, size and morphologies of samples were characterized by the transmission electron microscope (TEM, FEI Technai G2 F20), scanning electron microscope (SEM, JSM-5600LV), and high-resolution transmission electron microscope (HRTEM, FEI Technai G2 F20) operated at 200 kV along with selected area electron diffraction (SAED). Raman studies were carried out on a Horiba Jobin Yvon LabRAM HR800 spectrometer (France) with a 532-nm laser as the excitation source. The  $\text{N}_2$  adsorption-desorption isotherms were measured at liquid nitrogen temperature ( $-197^\circ\text{C}$ ) by using Micromeritics apparatus model ASAP 2020 equipment and the Brunauer–Emmett–Teller (BET) method. The  $\text{CO}_2$  adsorption isotherms were measured at  $0^\circ\text{C}$ .

### 2.3. Computational method

The density functional theory (DFT) calculation was performed by CP2K/Quickstep package [24]. Hubbard U correction was applied to d orbitals of Ti and Zn atoms with the corresponding U values set to 3.5 eV and 7.0 eV, respectively [24,25]. A 320 Ry cut off energy was used for auxiliary basis set of plane waves. The PBE exchange correlation functional was used in all calculations. The wave functions of valence electrons were expanded in terms of Gaussian function with molecularly optimized double-zeta polarized basis sets (m-DZVP) [26]. In addition, core electrons were described with the norm-conserving Goedecker, Teter, and Hutter (GTH) pseudopotentials [27].

### 2.4. Photocatalytic activity testing

By using as-obtained samples for photocatalytic  $\text{CO}_2$  reduction at ambient temperature under UV-light radiation (Philips Co., TUV 4 W/G4T5), their photocatalytic activities were evaluated. In a typical photocatalytic experiment, the quartz glass reactor was first heated at

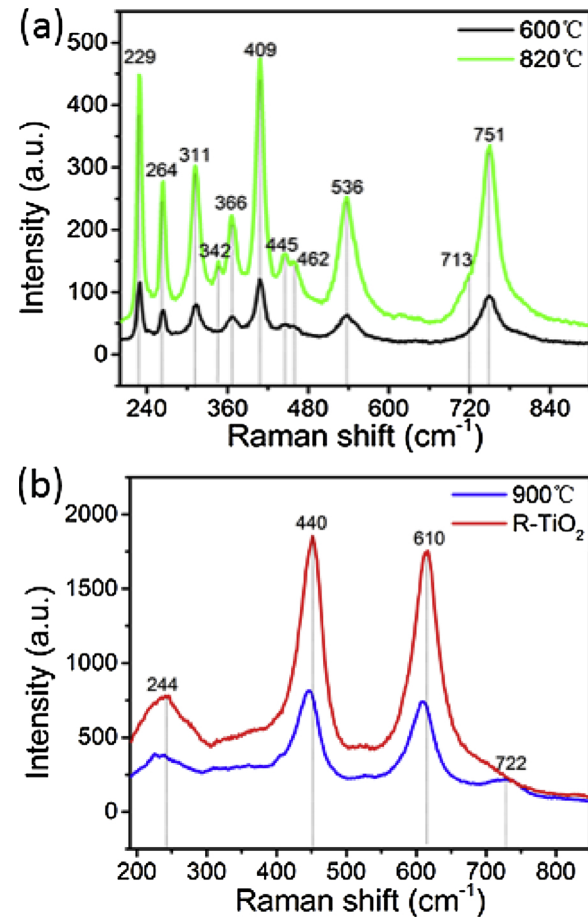


**Fig. 4.** Raman spectra of the synthesized samples: (a)  $\text{Zn}_2\text{Ti}_3\text{O}_8$  obtained at  $600^\circ\text{C}$  and  $\text{Zn}_2\text{Ti}_3\text{O}_8/\text{ZnTiO}_3$  obtained at  $820^\circ\text{C}$ . (b)  $\text{Zn}_2\text{TiO}_4/\text{R-TiO}_2$  obtained at  $900^\circ\text{C}$  and  $\text{R-TiO}_2$ .

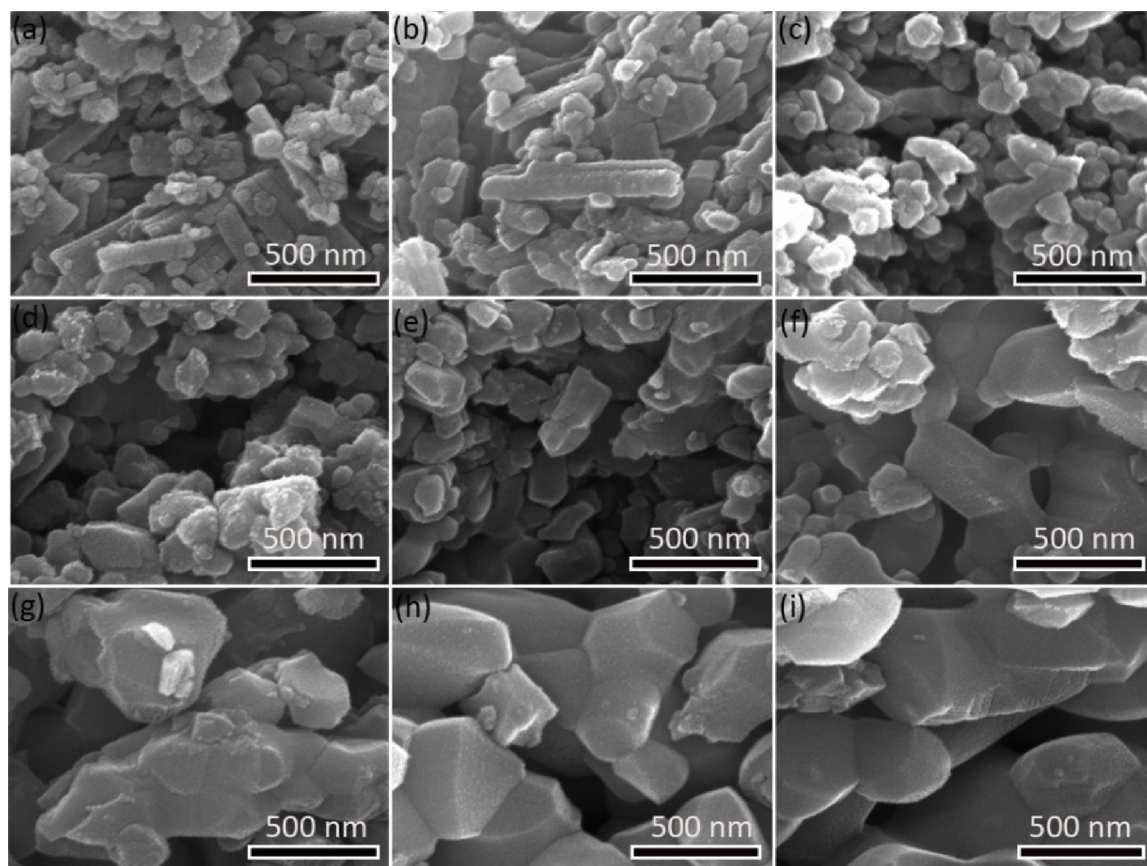


**Fig. 5.** Typical SEM images of the as-obtained products at different annealing temperatures (a) 600 °C (b) 700 °C (c) 750 °C (d) 800 °C (e) 820 °C (f) 850 °C (g) 880 °C (h) 900 °C and (i) 950 °C.

500 °C for 3 h in air to remove any possible traces of organic matter from the inner walls of reactor. Then, 50 mg of the as-prepared photocatalyst powder was dispersed in a 25-mL pyrex glass reactor with a silicone rubber septum. Subsequently, the whole system was subjected to vacuum degassing and then backfilling with pure CO<sub>2</sub> gas (99.995%) to remove the air inside. The evacuation-filling process was repeated four times, and then the reactor was backfilled with high-purity CO<sub>2</sub> (1 bar) after the last cycle. Finally, 20 µL of liquid deionized water was injected into the reactor with a microsyringe, and deionized water was gasified by heating with a hair dryer. Prior to illumination irradiation, magnetic stirring was performed in dark for 30 min for establishment of adsorption/desorption equilibrium. Then, photocatalytic reaction was carried out for 4 h under UV-light irradiation ( $\lambda = 254$  nm,  $4 \text{ W} \times 4 = 16\text{W}$ ). After the irradiation, for subsequent gas concentration analysis, 0.5 mL of gas was taken out from the glass reactor by a gas chromatography (GC-7890A, Shimadzu) equipped with a flame ionization detector (FID) and a capillary column (GC-GASPRO, 30 m × 0.320 mm). The outlet gas was determined to contain CO and CH<sub>4</sub>. The product gas was calibrated with a standard gas mixture, its identity was determined with the retention time, and it was then analyzed quantitatively with external standard method. In the test of the stability of photocatalyst, the photocatalytic reaction was evacuated at ambient temperature for 4 h and refilled with high-purity CO<sub>2</sub> and liquid deionized water in each cycle.

## 2.5. Electrochemical impedance spectra

An electrochemical impedance spectrometer (EIS) is generally used to characterize the interfacial electrochemical properties of electrodes. The EIS tests were carried out by a three-electrode electrochemical system in 5.0 mmol L<sup>-1</sup> Fe(CN)<sub>6</sub><sup>3-/4-</sup> mixture containing 0.1 mol L<sup>-1</sup>

KCl solution with saturated calomel electrode (SCE) and platinum (Pt) column as the reference electrode and counter electrode, respectively.

## 3. Results and discussion

**Fig. 1** shows the XRD patterns of thermally treated products of zinc titanate precursor obtained at different calcination temperatures between 600°C and 950°C. In **Fig. 1a**, the samples calcined at 600 and 700 °C only possess a cubic crystal structure as Zn<sub>2</sub>Ti<sub>3</sub>O<sub>8</sub> (PDF#13-0471), and it can be confirmed that both samples are pure cubic Zn<sub>2</sub>Ti<sub>3</sub>O<sub>8</sub> crystals. As the calcination temperature increased to 750 °C, hexagonal ZnTiO<sub>3</sub> (PDF#25-0671) began to be formed. This means that heterostructured Zn<sub>2</sub>Ti<sub>3</sub>O<sub>8</sub>/ZnTiO<sub>3</sub> nanohybrids can be obtained in situ. The peak intensities of ZnTiO<sub>3</sub> was continuously increased as calcination temperature-increased from 750 to 850°C (**Fig. 1b**). As the calcination temperature further increased from 850 to 950°C, cubic-spinel phase Zn<sub>2</sub>TiO<sub>4</sub> (PDF#25-1164) and R-TiO<sub>2</sub> (PDF#21-1276) were formed simultaneously, which were mainly resulted from the decomposition of Zn<sub>2</sub>Ti<sub>3</sub>O<sub>8</sub> and ZnTiO<sub>3</sub> [28]. In sum, by changing the temperature in the range of 600 – 950 °C, a series of zinc titanate-based heterostructured nanohybrids including Zn<sub>2</sub>Ti<sub>3</sub>O<sub>8</sub>/ZnTiO<sub>3</sub> and Zn<sub>2</sub>TiO<sub>4</sub>/R-TiO<sub>2</sub> can be prepared through a facile thermal annealing process. However, the XRD patterns suggest that pure ZnTiO<sub>3</sub> and Zn<sub>2</sub>TiO<sub>4</sub> were not formed in the temperature range of 600-950°C. This might be mainly because pure ZnTiO<sub>3</sub> is a special metastable phase and can easily decompose into Zn<sub>2</sub>TiO<sub>4</sub>, rutile-type TiO<sub>2</sub> and other phases at high temperature [29,30].

Furthermore, the surface chemical bonding and element binding energy (BE) of the samples were characterized by XPS (**Fig. 2**). For bare Zn<sub>2</sub>Ti<sub>3</sub>O<sub>8</sub>, the Ti 2p<sub>3/2</sub> and 2p<sub>1/2</sub> peaks centered at 458.74 eV and 464.52 eV, respectively, could be assigned to Ti<sup>4+</sup> valence state (**Fig. 2c**) [31,32], the Zn 2p<sub>3/2</sub> and Zn 2p<sub>1/2</sub> peaks positioned at

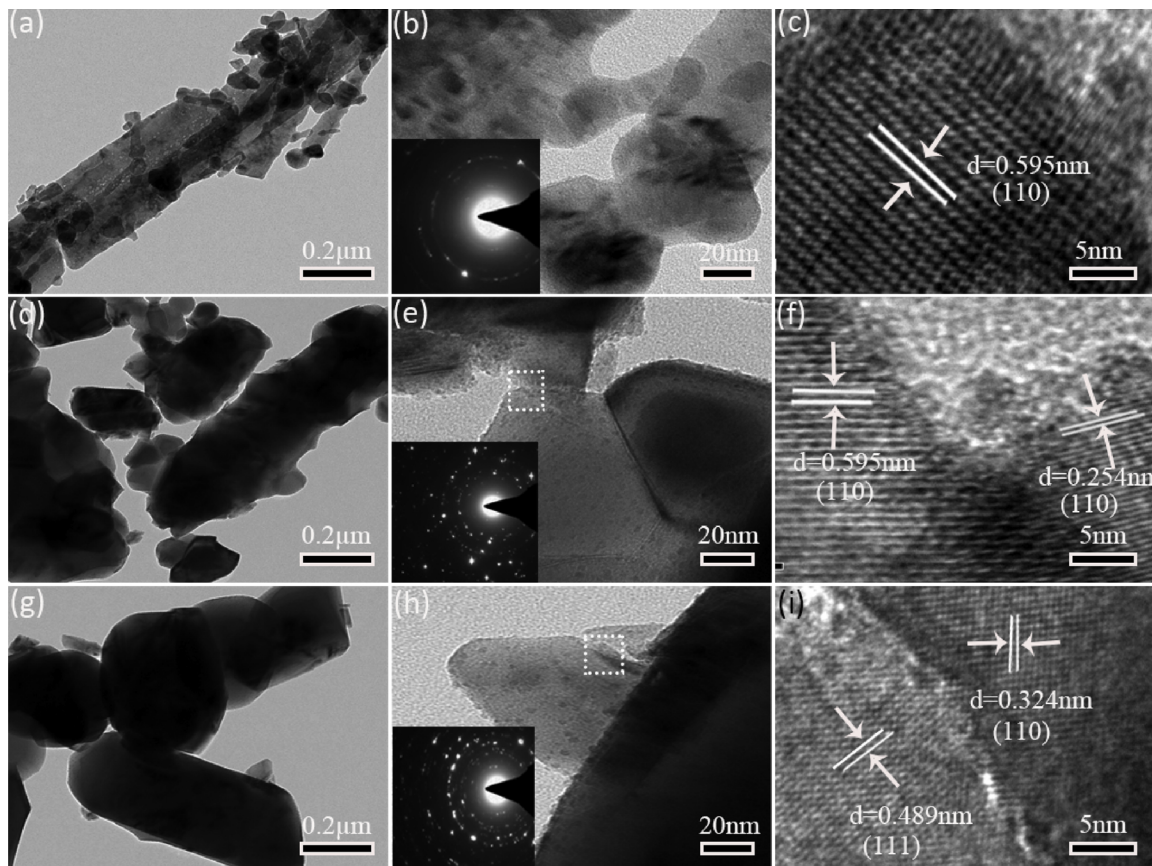


**Fig. 6.** Typical (a, b) low-magnification TEM and (c) high-resolution TEM images of the  $\text{Zn}_2\text{Ti}_3\text{O}_8$  obtained at  $600^\circ\text{C}$ . Typical (d, e) low-magnification TEM and (f) high-resolution TEM images of the  $\text{Zn}_2\text{Ti}_3\text{O}_8/\text{ZnTiO}_3$  obtained at  $820^\circ\text{C}$ . Typical (g, h) low-magnification and (i) high-resolution TEM images of the  $\text{Zn}_2\text{TiO}_4/\text{R-TiO}_2$  obtained at  $900^\circ\text{C}$ . Insets in panels (b), (e) and (h) are the corresponding SAED patterns.

1022.05 eV and 1045.06 eV (Fig. 2d), respectively, suggest the existence of  $\text{Zn}^{2+}$  valence state [33]. In comparison, for the  $\text{Zn}_2\text{Ti}_3\text{O}_8/\text{ZnTiO}_3$  heterostructure, the peaks of Ti 2p and Zn 2p synchronously shifted slightly toward lower BE, and similar result was also observed in the BE peaks of O 1s (Fig. 2b). The differences in element BE may be mainly attributed to the formation of  $\text{Zn}_2\text{Ti}_3\text{O}_8/\text{ZnTiO}_3$  heterostructure, which can lead to the changes of element chemical environments. In the XPS spectra of  $\text{BiVO}_4$  [34] and  $\text{CdS}$  [12] heterostructures, such phenomenon was also observed.

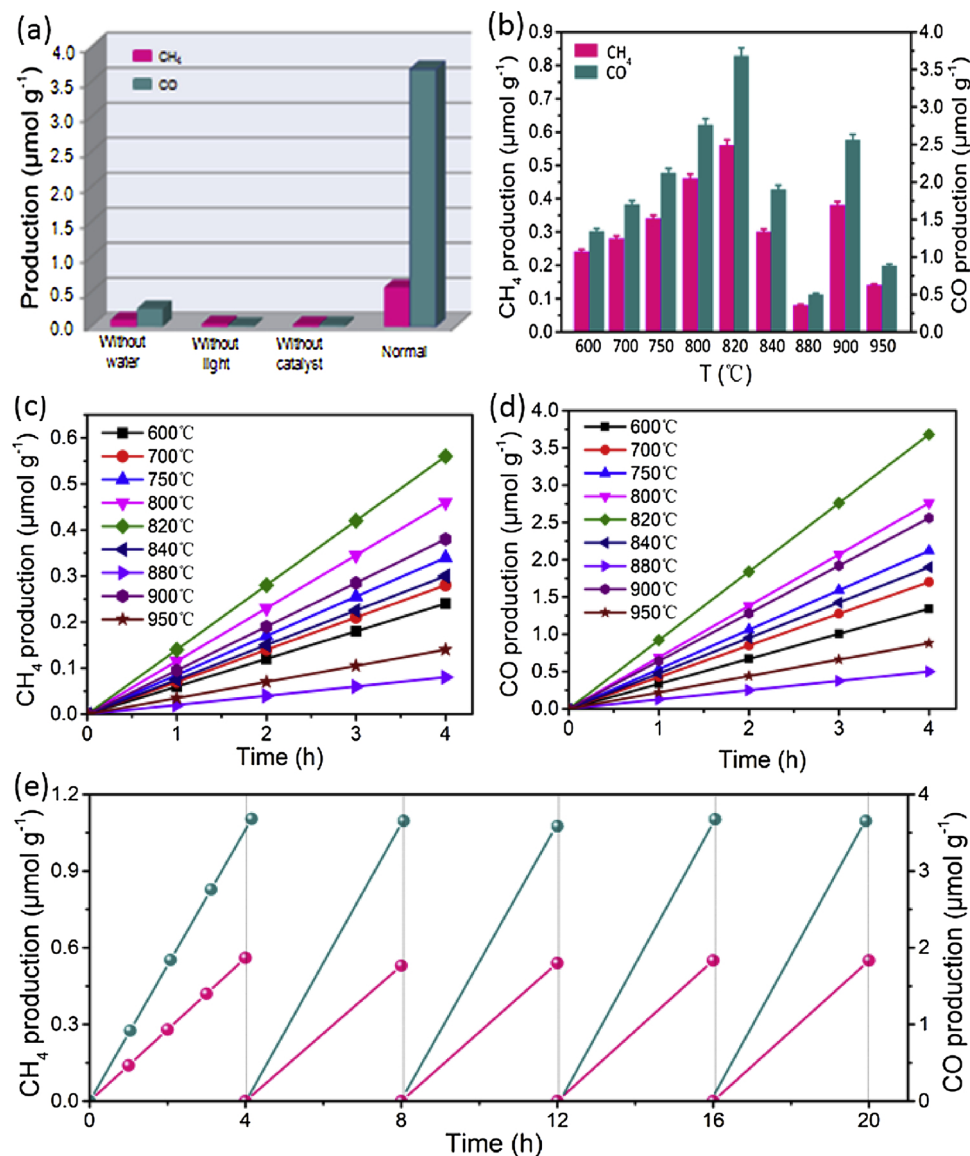
Compared with the XPS peaks of R-TiO<sub>2</sub> (Fig. 3), the XPS peaks of heterostructured  $\text{Zn}_2\text{TiO}_4/\text{R-TiO}_2$  sample shifted to higher BE. Specifically, the peak of O 1s shifted from 529.82 eV to 530.12 eV (Fig. 3b), which is probably due to the formation of Zn-O bond (Fig. 3d), usually located at around 530.0 eV [35]. In Fig. 3c, the peak of Ti 2p<sub>3/2</sub> shifted from 458.55 eV to 458.67 eV and the peak of Ti 2p<sub>1/2</sub> shifted from 464.28 eV to 464.41 eV. This is probably because the existence of Zn atoms leads to changes in the dispersion of electrons around Ti atoms.

Fig. 4a shows the Raman spectra of bare  $\text{Zn}_2\text{Ti}_3\text{O}_8$  and  $\text{Zn}_2\text{Ti}_3\text{O}_8/\text{ZnTiO}_3$  composite. Compared with bare  $\text{Zn}_2\text{Ti}_3\text{O}_8$ , the  $\text{Zn}_2\text{Ti}_3\text{O}_8/\text{ZnTiO}_3$  composite presents peaks at around 264, 342, 462 and  $713\text{ cm}^{-1}$  in its Raman spectra, which are attributed to the vibration modes of  $\nu_4(\text{LO})$ ,  $\nu_2(\text{LO}, \text{TO})$ ,  $\nu_1(\text{TO})$  and  $\nu_1(\text{LO})$ , respectively and are the characteristic peaks of hexagonal  $\text{ZnTiO}_3$ . It is also noted that most of the peaks for  $\text{Zn}_2\text{Ti}_3\text{O}_8/\text{ZnTiO}_3$  composite broadened and shifted towards higher frequencies. Fig. 4b shows the Raman spectra of bare R-TiO<sub>2</sub> and  $\text{Zn}_2\text{TiO}_4/\text{R-TiO}_2$  composite obtained at  $900^\circ\text{C}$ . Peaks at 244, 440 and  $610\text{ cm}^{-1}$  are attributed to those of R-TiO<sub>2</sub> [36,37]. For the  $\text{Zn}_2\text{TiO}_4/\text{R-TiO}_2$  sample, the peak at  $722\text{ cm}^{-1}$  can be ascribed to the spinel-structure  $\text{Zn}_2\text{TiO}_4$ , corresponding to the normal mode of representation A<sub>1g</sub> of the space group O<sub>h</sub><sup>7</sup> [38]. These results are well

consistent with the XRD analysis as discussed above.

The SEM images of samples obtained at various calcination temperatures are shown in Fig. 5. Fig. 5a displays the typical rod-shaped 1-D nanostructures of  $\text{Zn}_2\text{Ti}_3\text{O}_8$  obtained at  $600^\circ\text{C}$ , and their lengths typically range from 100 to 300 nm. The  $\text{Zn}_2\text{Ti}_3\text{O}_8$  sample obtained at  $700^\circ\text{C}$  was found to consist of nanorods coated with nanoparticles (Fig. 5b). As calcination temperature increased from 750 to  $850^\circ\text{C}$ , the rod-shaped structures gradually disappeared and many irregular particles and shredded nanorods of  $\text{Zn}_2\text{Ti}_3\text{O}_8/\text{ZnTiO}_3$  were formed (Fig. 5c-f). Notably, the particle sizes increase with increasing calcination temperature. As the calcination temperature further increased from 850 to  $950^\circ\text{C}$ , the as-obtained  $\text{Zn}_2\text{TiO}_4/\text{R-TiO}_2$  samples were found to consist of irregular particles with size of ca. 500 nm (Fig. 5g-i).

TEM images further reveal more details about the nanostructures of  $\text{Zn}_2\text{Ti}_3\text{O}_8$ ,  $\text{Zn}_2\text{Ti}_3\text{O}_8/\text{ZnTiO}_3$  and  $\text{Zn}_2\text{TiO}_4/\text{R-TiO}_2$  samples. Fig. 6a and b show the typical TEM images of  $\text{Zn}_2\text{Ti}_3\text{O}_8$  nanorods obtained at  $600^\circ\text{C}$ . The morphological characteristics of the sample are consistent with those revealed by SEM observation. The HRTEM image of the sample is presented in Fig. 6c. The distance between the adjacent lattice fringes is 0.595 nm, which can be assigned to the interplanar distance of the cubic  $\text{Zn}_2\text{Ti}_3\text{O}_8$  (110) plane. Fig. 6d and e show TEM images of  $\text{Zn}_2\text{Ti}_3\text{O}_8/\text{ZnTiO}_3$  composite obtained at  $820^\circ\text{C}$ . It was found that the sample is composed of nanorods and particles. To verify the  $\text{Zn}_2\text{Ti}_3\text{O}_8/\text{ZnTiO}_3$  heterostructure revealed by XRD results, HRTEM characterization was performed. As shown in Fig. 6f, explicit heterointerface between the  $\text{Zn}_2\text{Ti}_3\text{O}_8$  and  $\text{ZnTiO}_3$  phases can be observed, and the interplanar spacing of 0.595 nm and 0.254 nm correspond to (110) plane of  $\text{Zn}_2\text{Ti}_3\text{O}_8$  and (110) plane of  $\text{ZnTiO}_3$ , respectively. These results indicate the formation of  $\text{Zn}_2\text{Ti}_3\text{O}_8/\text{ZnTiO}_3$  heterostructure. For  $\text{Zn}_2\text{TiO}_4/\text{R-TiO}_2$  sample obtained at  $900^\circ\text{C}$ , the low magnification TEM images



**Fig. 7.** Photocatalytic performance: (a) The  $\text{CH}_4$  and  $\text{CO}$  yields under different conditions. (b) The  $\text{CH}_4$  and  $\text{CO}$  yields after 4 h of UV light irradiation. The time courses of (c) photocatalytic  $\text{CH}_4$  evolution and (d)  $\text{CO}$  production yield of various samples. (e) Cyclic use of photocatalyst for  $\text{CO}_2$  reduction.

(Fig. 6g and h) reveal rod-like particles, consistent with XRD result. As presented in Fig. 6i, the lattice spacing of 0.324 nm can be assigned to the (110) crystal plane of  $\text{Zn}_2\text{TiO}_4$  and the interplanar spacing of 0.489 nm corresponds the (111) plane of R- $\text{TiO}_2$ . Additionally, the selected-area electron diffraction (SAED) patterns of the three spots (see the insets in Fig. 6b, e and h) suggest the single-crystalline nature of the as-synthesized  $\text{Zn}_2\text{Ti}_3\text{O}_8$ ,  $\text{Zn}_2\text{Ti}_3\text{O}_8/\text{ZnTiO}_3$  and  $\text{Zn}_2\text{TiO}_4/\text{R-TiO}_2$  samples.

The zinc titanate-based heterostructures were employed as photocatalysts in  $\text{CO}_2$  reduction under UV-light illumination (Fig. 7). Fig. 7a shows no products were detected without light irradiation or in the absence of the photocatalyst. This result suggests that light and titanate-based photocatalyst are both necessary in  $\text{CO}_2$  reduction. In the absence of  $\text{H}_2\text{O}$ , it was observed that only a limited amount of  $\text{CH}_4$  and  $\text{CO}$  were generated under the catalysis of  $\text{Zn}_2\text{Ti}_3\text{O}_8/\text{ZnTiO}_3$  (obtained at 820°C). When water was added, the amount of  $\text{CO}$  and  $\text{CH}_4$  generated was significantly increased under UV-light irradiation. This result indicates that  $\text{H}_2\text{O}$  serves as hydrogen source and electron donor in the  $\text{CO}_2$  photoreduction system [2,12]. The photocatalytic performance of commercial anatase  $\text{TiO}_2$  (A- $\text{TiO}_2$ ) was also tested for comparison. The A- $\text{TiO}_2$  nanoparticles only showed a  $\text{CO}$  yield of ca. 0.93  $\mu\text{mol g}^{-1}$

(Figs. S2 and S3). Obviously, the zinc titanate-based heterostructured photocatalysts had a higher photocatalytic performance than A- $\text{TiO}_2$  in  $\text{CO}_2$  reduction. The photoreduction measurements, photocatalytic performances of a series of zinc titanate-based heterostructured photocatalysts were evaluated. As displayed in Fig. 7b, pure  $\text{Zn}_2\text{Ti}_3\text{O}_8$  merely showed a low  $\text{CO}$  of ca. 1.5  $\mu\text{mol g}^{-1}$  and a  $\text{CH}_4$  yield of ca. 0.23  $\mu\text{mol g}^{-1}$  after 4 h of UV-light irradiation, whereas the heterostructured  $\text{Zn}_2\text{Ti}_3\text{O}_8/\text{ZnTiO}_3$  prepared at 750–820°C showed  $\text{CO}$  and  $\text{CH}_4$  yields about two times of those pure  $\text{Zn}_2\text{Ti}_3\text{O}_8$ . Notably, the  $\text{Zn}_2\text{Ti}_3\text{O}_8/\text{ZnTiO}_3$  obtained at 820°C showed the highest photocatalytic performance, with  $\text{CH}_4$  and  $\text{CO}$  yields up to 0.56  $\mu\text{mol g}^{-1}$  and 3.68  $\mu\text{mol g}^{-1}$ , respectively. The  $\text{CH}_4$  and  $\text{CO}$  production yields of  $\text{Zn}_2\text{Ti}_3\text{O}_8/\text{ZnTiO}_3$  heterostructures obtained at 840°C were lower than those of  $\text{Zn}_2\text{Ti}_3\text{O}_8/\text{ZnTiO}_3$  heterostructures obtained at 820°C. These results can testify the vital role of heterogeneous interfaces endowed by various phase compositions in improving the photocatalytic performance of photocatalyst. The results also demonstrate that the co-existence of optimized phase junctions between  $\text{Zn}_2\text{Ti}_3\text{O}_8$  and  $\text{ZnTiO}_3$  is of great importance to effectively enhance the photocatalytic performance of photocatalyst.

In addition, the photocatalytic performance of  $\text{Zn}_2\text{TiO}_4/\text{R-TiO}_2$  heterostructure was evaluated. For comparison, the photocatalytic

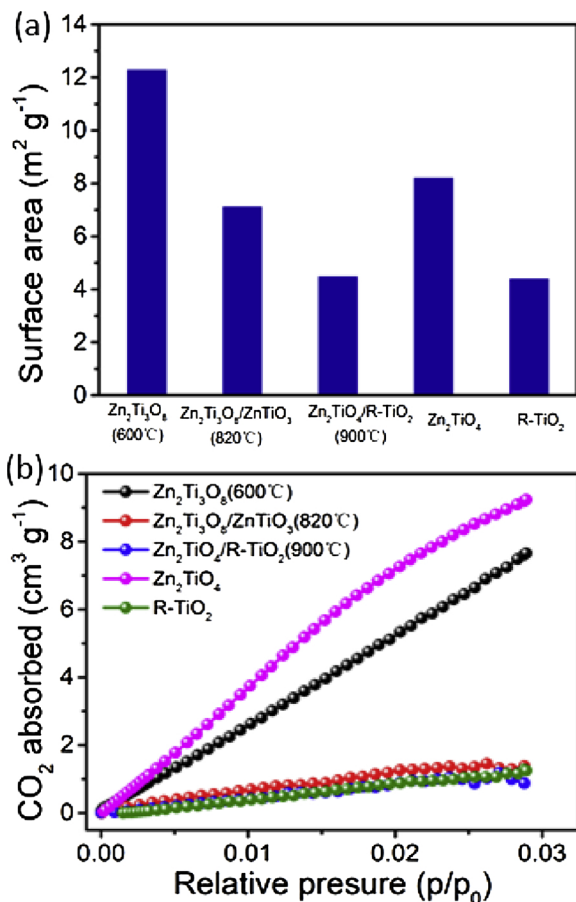


Fig. 8. The specific surface area (a) and  $\text{CO}_2$  adsorption isotherms (b) of the as-prepared samples.

performance of R-TiO<sub>2</sub>, Zn<sub>2</sub>TiO<sub>4</sub>, A-TiO<sub>2</sub> and R-TiO<sub>2</sub>+Zn<sub>2</sub>TiO<sub>4</sub> (prepared by physical mixing) were also determined. The yields of CH<sub>4</sub> and CO under the catalysis of R-TiO<sub>2</sub>, Zn<sub>2</sub>TiO<sub>4</sub>, A-TiO<sub>2</sub> and R-TiO<sub>2</sub>+Zn<sub>2</sub>TiO<sub>4</sub> mixture are shown in Fig. S2. Pure R-TiO<sub>2</sub> shows no photocatalytic activity. The CO yield of A-TiO<sub>2</sub> was only 0.93  $\mu\text{mol g}^{-1}$ . Furthermore, Zn<sub>2</sub>TiO<sub>4</sub> and R-TiO<sub>2</sub>/Zn<sub>2</sub>TiO<sub>4</sub> composite obtained by physical mixing also showed poor photocatalytic activities in CO<sub>2</sub> photoreduction. However, the maximal CH<sub>4</sub> and CO yields were achieved under the catalysis of heterostructured Zn<sub>2</sub>TiO<sub>4</sub>/R-TiO<sub>2</sub> (calcined at 900°C) and were 0.38  $\mu\text{mol g}^{-1}$  and 2.56  $\mu\text{mol g}^{-1}$ , respectively (Fig. 7b). Fig. 7c and d show the CH<sub>4</sub> and CO yields changing with illumination time under the catalysis of various photocatalysts. It was found that the amount of products (CH<sub>4</sub> and CO) increased linearly with irradiation time. As compared with other catalysts, the obtained Zn<sub>2</sub>Ti<sub>3</sub>O<sub>8</sub>/ZnTiO<sub>3</sub> (calcined at 820 °C) and Zn<sub>2</sub>TiO<sub>4</sub>/R-TiO<sub>2</sub> (calcined at 900°C) exhibited higher photocatalytic performance in the conversion of CO<sub>2</sub> to CH<sub>4</sub> and CO in the presence of water.

As a photocatalyst, reusability and stability are important factors for practical applications. In order to investigate the durability of the photocatalyst Zn<sub>2</sub>Ti<sub>3</sub>O<sub>8</sub>/ZnTiO<sub>3</sub> (calcined at 820°C) was cyclically used for five times in CO<sub>2</sub> reduction. As shown in Fig. 7e, the photocatalytic activity of the photocatalyst did not decrease after five successive cycles, and the amount of products (CH<sub>4</sub> and CO) almost increased linearly with increasing irradiation time per cycle. These results confirm the high stability of zinc titanate-based heterostructures.

According to the SEM results (Fig. 5), the particle sizes of the prepared samples increase with increasing calcining temperature. The BET specific surface areas of the products decreased from 12.4 to 4.5  $\text{m}^2 \text{g}^{-1}$  as calcining temperature increases from 600 to 900 °C (Figs. S4 and 8 a). Combining the results in Figs. 5, 8a, S2, S3 and 7 b, we can find that the

photocatalytic activities of zinc titanate-based heterostructures are not directly related to their size or specific surface area. In addition, the amount of CO<sub>2</sub> adsorbed on the photocatalysts was measured by the BET method at 0°C (Fig. 8b). The results show that the CO<sub>2</sub> adsorption capabilities of these photocatalysts are not consistent with the photocatalytic activity results reported above (Fig. 7b). This means that the enhanced photocatalytic activity of zinc titanate-based composites cannot be attributed to their CO<sub>2</sub> adsorption performance either. These results suggest that the surface-phase junctions may play a dominant role in promoting photogenerated charge separation and migration in the reaction of CO<sub>2</sub> with H<sub>2</sub>O.

Diffuse reflectance spectroscopy (DRS) technique is one of the powerful tools for immediately observing the optical absorption properties of semiconductors from UV to visible light. In order to reveal the band gap energy E<sub>g</sub> of zinc titanate-based samples, the UV-vis absorption spectra were obtained (Fig. 9a). According to the Kubelka-Munk equation:  $\text{chv} = A(\text{chv}-E_g)^n$  [39], it can be deduced that the samples obtained at 600, 820 and 900 °C and R-TiO<sub>2</sub> have a band gap energy E<sub>g</sub> of ca. 3.71, 3.62, 3.44 and 3.02 eV, respectively, corresponding to optical absorption edges of ca. 334, 342, 360 and 410 nm, respectively. Particularly, the DRS spectra of samples prepared at 820 and 900 °C both exhibit a shoulder peak at 350–400 nm, which may be due to that the samples were both composed of two different phases. The XPS valence band spectra of samples obtained are shown in Fig. 9b. It was estimated that the valence band potentials (E<sub>VB</sub>) of samples obtained at 600 °C, 820 °C, and 900 °C and R-TiO<sub>2</sub> are ca. 2.68, 2.67, 2.39, and 2.65 eV, respectively. Therefore, the conduction band potential (E<sub>CB</sub>) of above samples are about -1.03, -0.95, -1.05, and -0.37 eV, respectively, obtained by E<sub>CB</sub> = E<sub>VB</sub> - E<sub>g</sub>. As shown in Fig. S4, the E<sub>g</sub> and E<sub>VB</sub> of Zn<sub>2</sub>TiO<sub>4</sub> obtained at high temperature are 3.70 eV and 2.45 eV, and the E<sub>CB</sub> of Zn<sub>2</sub>TiO<sub>4</sub> is -1.25 eV. The E<sub>CB</sub> and E<sub>VB</sub> values are -0.46 eV and +3.19 eV for cubic ZnTiO<sub>3</sub>, respectively [40]. It is worth noting that the redox potential of CO/CO<sub>2</sub> is -0.53 V vs. NHE at pH 7.0 [41], thus products prepared at 600, 820, and 900°C and Zn<sub>2</sub>TiO<sub>4</sub> can help transform CO<sub>2</sub> and H<sub>2</sub>O to CO and CH<sub>4</sub>, but ZnTiO<sub>3</sub> and R-TiO<sub>2</sub> cannot help transform CO<sub>2</sub> to CO. This was also demonstrated through the experimental results reported above (Figs. 7 and S5).

To characterize the interfacial electrochemical properties of electrodes, an electrochemical impedance spectrum (EIS) is generally used. Commonly, the smaller arc in an EIS Nyquist plot indicates a smaller charge-transfer resistance on the electrode surface [42,43]. Fig. 9c shows that the relationship between the arc sizes of the two electrodes is Zn<sub>2</sub>Ti<sub>3</sub>O<sub>8</sub>/ZnTiO<sub>3</sub> < Zn<sub>2</sub>Ti<sub>3</sub>O<sub>8</sub>. This indicates that the Zn<sub>2</sub>Ti<sub>3</sub>O<sub>8</sub>/ZnTiO<sub>3</sub> heterostructure exhibits lower charge-transfer resistance than Zn<sub>2</sub>Ti<sub>3</sub>O<sub>8</sub> [42,43]. Similarly, as shown in Fig. 9d, the EIS spectra of Zn<sub>2</sub>TiO<sub>4</sub>/R-TiO<sub>2</sub> present a smaller arc than those of the bare R-TiO<sub>2</sub>, suggesting that Zn<sub>2</sub>TiO<sub>4</sub>/R-TiO<sub>2</sub> heterostructure exhibit lower charge-transfer resistance [44,45]. It is important to note that the EIS results of these heterostructured samples are consistent with the photocatalytic activity results reported above (Fig. 7). Therefore, the zinc titanate-based heterostructures can effectively reduce the rapid recombination of electron-hole pairs within photocatalytic materials. As a result, more effective charge separation and transfer as well as higher photocatalytic performance are achieved.

In order to analyze in depth the working mechanism of the heterostructures prepared, the band gap structures of Zn<sub>2</sub>Ti<sub>3</sub>O<sub>8</sub>/ZnTiO<sub>3</sub> and Zn<sub>2</sub>TiO<sub>4</sub>/R-TiO<sub>2</sub> were further studied. According to the above DRS and valence-band XPS spectra results, we propose here a possible route of CO<sub>2</sub> reduction, as shown in scheme 1.

The reduction of CO<sub>2</sub> usually proceeds in the presence of water. Commonly, the reduction potential of CO<sub>2</sub> (i.e., E<sup>0</sup>(CO<sub>2</sub>/CO) = -0.53 V vs. NHE at pH = 7.0) and the oxidation potential of H<sub>2</sub>O (i.e., E<sup>0</sup>(O<sub>2</sub>/H<sub>2</sub>O) = 0.82 V vs. NHE at pH = 7.0) should be considered to meet requirements of half-reaction of CO<sub>2</sub> reduction and half-reaction of water oxidation simultaneously [1,9]. On the basis of the detailed analysis of the band edge positions above (Fig. 9 and Scheme

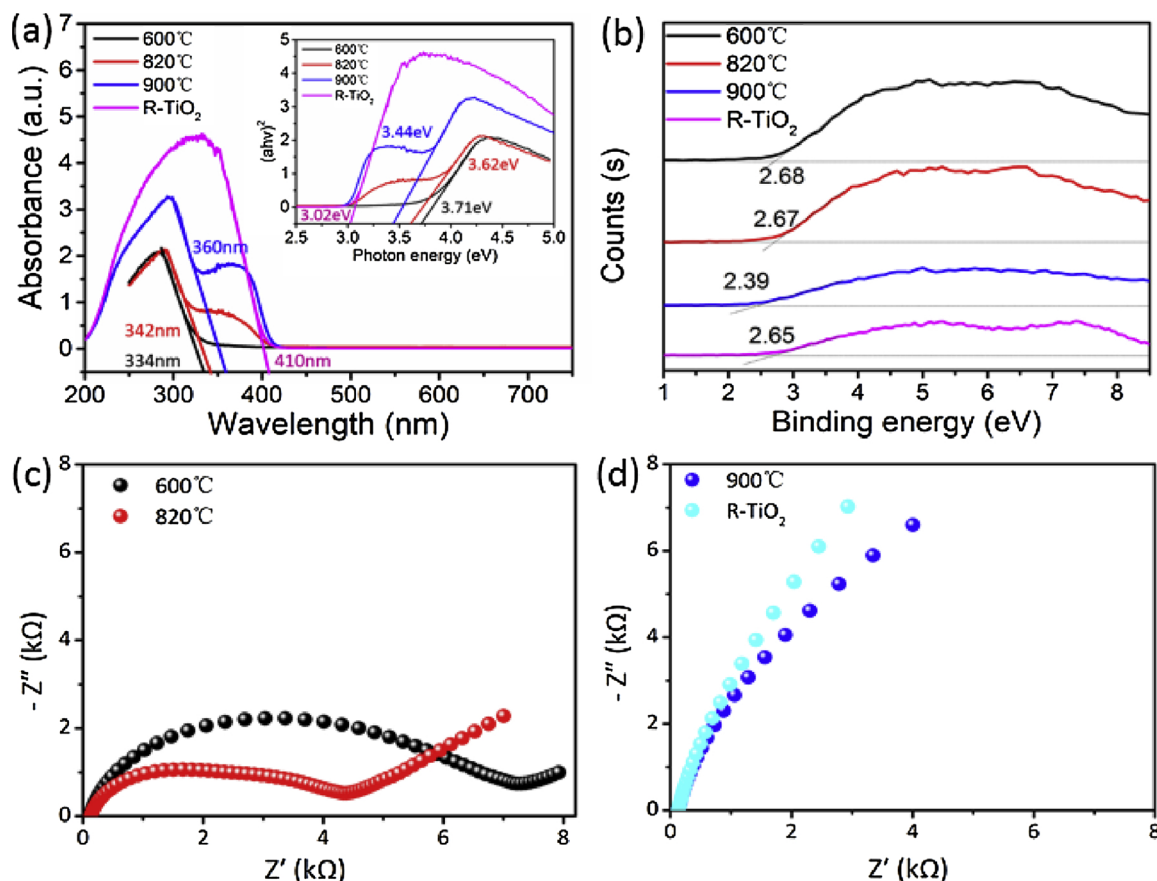
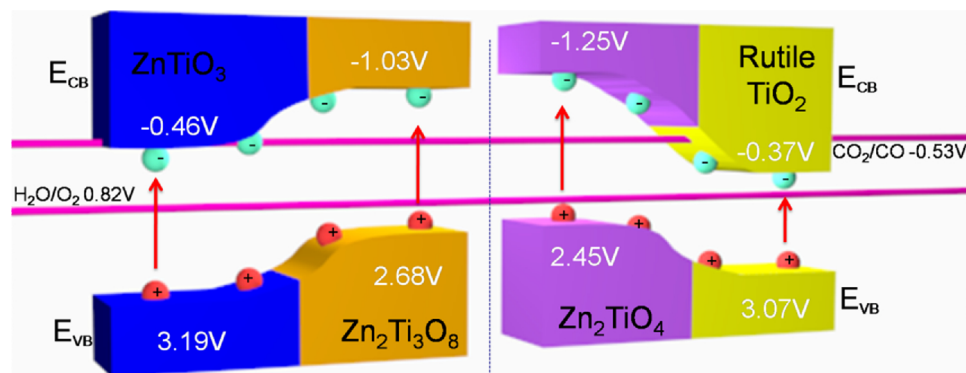


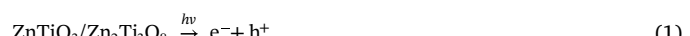
**Fig. 9.** (a) Diffuse absorption spectra of the samples obtained at 600 °C, 820 °C and 900 °C and R-TiO<sub>2</sub> (inset is the optical band gap energy Eg of corresponding samples). (b) Valence-band XPS spectra of corresponding samples. (c-d) Electrochemical impedance spectra of the samples obtained.



**Scheme 1.** Schematic illustration of charge separation and transfer pathway in Zn<sub>2</sub>Ti<sub>3</sub>O<sub>8</sub>/ZnTiO<sub>3</sub> heterostructure (left) and Zn<sub>2</sub>TiO<sub>4</sub>/R-TiO<sub>2</sub> heterostructure (right).

1), ZnTiO<sub>3</sub> and R-TiO<sub>2</sub> cannot catalyze the photoreduction of CO<sub>2</sub> to CO because the E<sub>CB</sub> potentials of ZnTiO<sub>3</sub> (-0.46 V vs. NHE) and R-TiO<sub>2</sub> (-0.37 V vs. NHE) are more positive than the standard redox potential E<sup>0</sup>(CO<sub>2</sub>/CO) = -0.53 V vs. NHE. However, Zn<sub>2</sub>Ti<sub>3</sub>O<sub>8</sub> (E<sub>CB</sub> = -1.03 V vs. NHE) and Zn<sub>2</sub>TiO<sub>4</sub> (E<sub>CB</sub> = -1.25 V vs. NHE) are active phases and can catalyze CO<sub>2</sub> reduction. To take Zn<sub>2</sub>Ti<sub>3</sub>O<sub>8</sub>/ZnTiO<sub>3</sub> as an example, the electrons and holes are generated at the Zn<sub>2</sub>Ti<sub>3</sub>O<sub>8</sub>/ZnTiO<sub>3</sub> photocatalyst (eq. 1). Thermodynamically, in addition to the photogenerated electrons, the effect of the simultaneously photoinduced holes should be involved. The valence band of most semiconductors (e.g., Zn<sub>2</sub>Ti<sub>3</sub>O<sub>8</sub> (E<sub>VB</sub> = 2.68 V vs. NHE)) is located well below the oxidation potential of water, whereas eq. 2 gives a value of 2.32 V (E<sup>0</sup>(H<sub>2</sub>O/OH) = 2.32 V vs. NHE) [46,47]. Therefore, in our case, at the surface the holes (h<sup>+</sup>) can react with the adsorbed H<sub>2</sub>O molecule to produce hydroxyl radicals (·OH) and protons (H<sup>+</sup>) (eq. 2) [2], and the electrons are involved in

reduction reaction with CO<sub>2</sub> to produce CH<sub>4</sub> and CO and oxidation reaction with H<sub>2</sub>O to produce H<sup>+</sup>. The formation of CO and CH<sub>4</sub> requires 2H<sup>+</sup>/2e<sup>-</sup> and 8H<sup>+</sup>/8e<sup>-</sup> [48], respectively, according to eqs. (3) and (4). The proposed reactions involved in the CO<sub>2</sub> photoreduction to produce CH<sub>4</sub> and CO can be described by eqs. (1)–(4).



Upon the UV-light irradiation, both ZnTiO<sub>3</sub> and Zn<sub>2</sub>Ti<sub>3</sub>O<sub>8</sub> components in the Zn<sub>2</sub>Ti<sub>3</sub>O<sub>8</sub>/ZnTiO<sub>3</sub> heterostructure are excited to generate charge carriers in their valence band (VB) and conduction band (CB),

respectively. Those components alone present poor photocatalytic performance owing to the direct recombination of most photo-induced electron-hole pairs. After the  $\text{Zn}_2\text{Ti}_3\text{O}_8/\text{ZnTiO}_3$  heterojunction was constructed, the photoelectrons of  $\text{Zn}_2\text{Ti}_3\text{O}_8$  in the CB could readily migrate to the CB position of  $\text{ZnTiO}_3$  through the interface electronic field, resulting in effective separation of charges through heterojunction. Meanwhile, the photoelectrons and holes are gathered on CB position of  $\text{ZnTiO}_3$  and VB position of  $\text{Zn}_2\text{Ti}_3\text{O}_8$ , respectively. This means that the synergistic effect of the  $\text{Zn}_2\text{Ti}_3\text{O}_8/\text{ZnTiO}_3$  heterostructure may promote efficient separation and transfer of photoinduced charges and therefore restrain the recombination of photogenerated electron – hole pairs, resulting in an enhanced photocatalytic activity in  $\text{CO}_2$ -reduction. In view of the above results, the approximate band-edge positions of the  $\text{Zn}_2\text{Ti}_3\text{O}_8$ ,  $\text{ZnTiO}_3$ ,  $\text{Zn}_2\text{TiO}_4$  and  $\text{R-TiO}_2$  are displayed in **scheme 1**, demonstrating that the  $\text{Zn}_2\text{Ti}_3\text{O}_8/\text{ZnTiO}_3$  heterostructure and  $\text{Zn}_2\text{TiO}_4/\text{R-TiO}_2$  heterostructure facilitate directed charge carrier transport and suppress charge recombination by Ti-O bonding at the atomic level, thus promoting  $\text{CO}_2$  reduction [49].

To gain more atomic insight into the electron-hole transport mechanism, the electronic structures of  $\text{Zn}_2\text{Ti}_3\text{O}_8/\text{ZnTiO}_3$  and  $\text{Zn}_2\text{TiO}_4/\text{R-TiO}_2$  were studied by density functional theory (DFT) calculations (Figs. S6 and S7). The calculated densities of states (DOS) of individual  $\text{Zn}_2\text{Ti}_3\text{O}_8$ ,  $\text{ZnTiO}_3$ ,  $\text{Zn}_2\text{TiO}_4$ ,  $\text{R-TiO}_2$ ,  $\text{Zn}_2\text{Ti}_3\text{O}_8/\text{ZnTiO}_3$  and  $\text{Zn}_2\text{TiO}_4/\text{R-TiO}_2$  reveal typical semiconductor characteristics with band-gap of less than 4 eV (Table S1). As for the  $\text{Zn}_2\text{Ti}_3\text{O}_8/\text{ZnTiO}_3$  heterostructure, the band gap is about 3.50 eV. As shown in the Fig. S7e, the contribution of Zn atoms is smaller than that of Ti atoms. In comparison with pure  $\text{Zn}_2\text{Ti}_3\text{O}_8$  and  $\text{ZnTiO}_3$ ,  $\text{Zn}_2\text{Ti}_3\text{O}_8/\text{ZnTiO}_3$  shows reduced band gap, implying that the heterostructure can increase the wavelength of absorbed light, thereby achieving higher photoconversion efficiency. As for the DOS of  $\text{R-TiO}_2/\text{Zn}_2\text{TiO}_4$  heterostructure, the band gap is about 3.0 eV, which is close to the experiment value, and the conduction band and the valence band are mainly composed by the Ti and O atoms. Hence, based on the experimental analysis and theoretical calculations, we can conclude that the heterostructure is much better for the separation of electrons and holes than the others.

#### 4. Conclusions

In sum, we reported the synthesis of  $\text{Zn}_2\text{Ti}_3\text{O}_8/\text{ZnTiO}_3$  and  $\text{Zn}_2\text{TiO}_4/\text{R-TiO}_2$  heterostructures via a facile hydrothermal reaction of butyl titanate with zinc acetate, followed by high-temperature calcinations under air flow. Subsequent detailed investigations show that the heterostructured nanohybrids possess explicit heterointerfaces and tunable band edges. When used as photocatalysts towards the reduction of  $\text{CO}_2$  with  $\text{H}_2\text{O}$  under UV-light irradiation, the nanocrystalline  $\text{Zn}_2\text{Ti}_3\text{O}_8/\text{ZnTiO}_3$  and  $\text{Zn}_2\text{TiO}_4/\text{R-TiO}_2$  heterostructures show high photocatalytic performance, with  $\text{CH}_4$  and CO yields of  $0.56 \mu\text{mol g}^{-1}$  and  $3.68 \mu\text{mol g}^{-1}$ , as well as  $0.38 \mu\text{mol g}^{-1}$  and  $2.56 \mu\text{mol g}^{-1}$ , respectively, after 4 h of UV-light irradiation. The band gap structures and the working mechanisms of  $\text{Zn}_2\text{Ti}_3\text{O}_8/\text{ZnTiO}_3$  and  $\text{Zn}_2\text{TiO}_4/\text{R-TiO}_2$  heterostructures were proposed. The present work indicates that the enhanced photoactivity may be resulted from the efficient separation of photoinduced electron-hole pairs derived from the constructed zinc titanate heterostructures. This work would provide a significant strategy to effectively convert  $\text{CO}_2$  into fuels by using rationally designed heterostructures.

#### Acknowledgements

This research was supported by the National Natural Science Foundation of China (Grant No. 21862015, 21463019, 21865022), the National First-rate Discipline Project of Ningxia (No. NXYLXK2017A04), and the Natural Science Foundation of Ningxia Province (2018AAC03032).

#### Appendix A. Supplementary data

Supplementary material related to this article can be found, in the online version, at doi:<https://doi.org/10.1016/j.apcatb.2019.117800>.

#### References

- [1] W.G. Tu, Y. Zhou, Z.G. Zou, Photocatalytic conversion of  $\text{CO}_2$  into renewable hydrocarbon fuels: state-of-the-art accomplishment, challenges, and prospects, *Adv. Mater.* 26 (2014) 4607–4626, <https://doi.org/10.1002/adma.201400087>.
- [2] Y. Izumi, Recent advances in the photocatalytic conversion of carbon dioxide to fuels with water and/or hydrogen using solar energy and beyond, *Coord. Chem. Rev.* 257 (2013) 171–186, <https://doi.org/10.1016/j.ccr.2012.04.018>.
- [3] S.C. Roy, O.K. Varghese, M. Paulose, C.A. Grimes, Towards solar fuels: photocatalytic Conversion of carbon dioxide to hydrocarbons, *ACS Nano Lett.* 4 (2010) 1259–1278, <https://doi.org/10.1021/nm901542z>.
- [4] G. Sneddon, A. Greenaway, H.H.P. Yiu, The potential applications of nanoporous materials for the adsorption, separation, and catalytic conversion of carbon dioxide, *Adv. Energy Mater.* 4 (2014) 281–286, <https://doi.org/10.1002/aenm.201301873>.
- [5] M. Halimann, Photoelectrochemical reduction of aqueous carbon dioxide on p-type gallium phosphide in liquid junction solar cells, *Nature* 275 (1978) 115–116, <https://doi.org/10.1038/275115a0>.
- [6] M. Yamamoto, T. Yoshida, N. Yamamoto, T. Nomoto, Y. Yamamoto, S. Yagi, H. Yoshida, Photocatalytic reduction of  $\text{CO}_2$  with water promoted by Ag clusters in  $\text{Ag}/\text{Ga}_2\text{O}_3$  photocatalysts, *J. Mater. Chem. A* 3 (2015) 16810–16816, <https://doi.org/10.1039/C5TA04815J>.
- [7] X.C. Jiao, Z.W. Chen, X.D. Li, Y.F. Sun, S. Gao, W.S. Yan, C.M. Wang, Q. Zhang, Y. Lin, Y. Luo, Y. Xie, Partially oxidized  $\text{SnS}_2$  atomic layers achieving efficient visible-light-driven  $\text{CO}_2$  reduction, *J. Am. Chem. Soc.* 139 (2017) 7586–7594, <https://doi.org/10.1021/jacs.7b10287>.
- [8] S.J. Xie, Y. Wang, Q.H. Zhang, W.P. Deng, Y. Wang,  $\text{SrNb}_2\text{O}_6$  nanoplates as efficient photocatalysts for the preferential reduction of  $\text{CO}_2$  in the presence of  $\text{H}_2\text{O}$ , *Chem. Commun.* 51 (2015) 3430–3433, <https://doi.org/10.1039/c4cc10241j>.
- [9] S.N. Habersreuter, L. Schmidt-Mende, J.K. Stolarczyk, Photocatalytic reduction of  $\text{CO}_2$  on  $\text{TiO}_2$  and other semiconductors, *Angew. Chem. Int. Ed.* 52 (2013) 7372–7408, <https://doi.org/10.1002/anie.201207199>.
- [10] Y. Qu, X. Duan, Progress, challenge and perspective of heterogeneous photocatalysts, *Chem. Soc. Rev.* 42 (2013) 2568–2580, <https://doi.org/10.1039/C2CS35355E>.
- [11] H.L. Wang, L.S. Zhang, Z.G. Chen, J.Q. Hu, S.J. Li, Z.H. Wang, J.S. Liu, X.C. Wang, ChemInform abstract: semiconductor heterojunction photocatalysts: design, construction, and photocatalytic performances, *Chem. Soc. Rev.* 43 (2014) 5234–5244, <https://doi.org/10.1039/C4CS00126E>.
- [12] Y. Chai, J.X. Lu, L. Li, D.L. Li, M. Li, J. Liang, TEOA-induced in situ formation of wurtzite and zinc-blende  $\text{CdS}$  heterostructures as a highly active and long-lasting photocatalyst for converting  $\text{CO}_2$  into solar fuel, *Catal. Sci. Technol.* 8 (2018) 2697–2706, <https://doi.org/10.1039/C8CY00274F>.
- [13] Y. Wang, Z.Z. Zhang, L. Zhang, Z.B. Luo, J.N. Shen, H.X. Lin, J.L. Long, J.C.S. Wu, X.Z. Fu, X.X. Wang, C. Li, Visible-light driven overall conversion of  $\text{CO}_2$  and  $\text{H}_2\text{O}$  to  $\text{CH}_4$  and  $\text{O}_2$  on 3D-SiC@2D-MoS<sub>2</sub> heterostructure, *J. Am. Chem. Soc.* 141 (2019) 7660–7664, <https://doi.org/10.1021/jacs.8b09344>.
- [14] Y.M. He, L.H. Zhang, B.T. Teng, M.H. Fan, New application of z-scheme  $\text{Ag}_3\text{PO}_4/\text{g-C}_3\text{N}_4$  composite in converting  $\text{CO}_2$  to fuel, *Environ. Sci. Technol.* 49 (2015) 649–656, <https://doi.org/10.1021/es5046309>.
- [15] Y. Qu, W. Zhou, Z.Y. Ren, G.F. Wang, B.J. Jiang, H.G. Fu, Facile synthesis of porous  $\text{Zn}_2\text{Ti}_3\text{O}_8$  nanorods for photocatalytic overall water splitting, *ChemCatChem* 6 (2014) 2258–2262, <https://doi.org/10.1002/cctc.201402184>.
- [16] J.B.M. Goodall, S. Kellie, D. Illsley, R. Lines, J.C. Knowles, J.A. Darr, Optical and photocatalytic behaviours of nanoparticles in the  $\text{Ti-Zn-O}$  binary system, *RSC Adv.* 4 (2014) 31799–31809, <https://doi.org/10.1039/c3ra48030e>.
- [17] J.Z. Kong, A.D. Li, H.F. Zhai, H. Li, Q.Y. Yan, J. Ma, D. Wu, Preparation, characterization and photocatalytic properties of  $\text{ZnTiO}_3$  powders, *J. Hazard. Mater.* 171 (2009) 918–923, <https://doi.org/10.1016/j.jhazmat.2009.06.092>.
- [18] T. Surendar, S. Kumar, V. Shanker, Influence of La-doping on phase transformation and photocatalytic properties of  $\text{ZnTiO}_3$  nanoparticles synthesized via modified sol-gel method, *Phys. Chem. Chem. Phys.* 16 (2013) 728–735, <https://doi.org/10.1039/C3CP53855A>.
- [19] G.L. Zhou, H.Q. Sun, S.B. Wang, H.M. Ang, M.O. Tade, Titanate supported cobalt catalysts for photochemical oxidation of phenol under visible light irradiations, *Sep. Purif. Technol.* 80 (2011) 626–634, <https://doi.org/10.1016/j.seppur.2011.06.021>.
- [20] J. Yang, J.H. Swisher, The phase stability of  $\text{Zn}_2\text{Ti}_3\text{O}_8$ , *Mater. Charact.* 37 (1996) 153–159, [https://doi.org/10.1016/s1044-5803\(96\)00098-8](https://doi.org/10.1016/s1044-5803(96)00098-8).
- [21] M. Zhao, B.P. Bastakoti, Y.Q. Li, H. Xu, J.H. Ye, Z.W. Liu, Y. Yamauchi, Mesoporous  $\text{TiO}_2/\text{Zn}_2\text{Ti}_3\text{O}_8$  hybrid films by polymeric micelle assembly, *Chem. Commun.* 51 (2015) 14582–14585, <https://doi.org/10.1039/c5cc04903b>.
- [22] J.C. Conesa, Band structures and nitrogen doping effects in zinc titanate photocatalysts, *Catal. Today* 208 (2013) 11–18, <https://doi.org/10.1016/j.cattod.2012.08.039>.
- [23] Y.R. Tao, Y.L. Zhang, L.L. Wen, X.C. Wu, Synthesis, characterization and gas-sensing properties of sodium titanate nanobelts, *Chin. J. Inorg. Chem.* 24 (2008) 1570–1575, <https://doi.org/10.3724/SP.J.1001.2008.01707>.
- [24] J. Vandevondele, M. Krack, F. Mohamed, M. Parrinello, T. Chassaing, J. Hutter, Quickstep: fast and accurate density functional calculations using a mixed Gaussian and plane waves approach, *Comput. Phys. Commun.* 167 (2005) 103–128, <https://doi.org/10.1016/j.cpc.2005.02.003>.

- [doi.org/10.1016/j.cpc.2004.12.014](https://doi.org/10.1016/j.cpc.2004.12.014).
- [25] J. Vandevondele, J. Hutter, Gaussian basis sets for accurate calculations on molecular systems in gas and condensed phases, *J. Chem. Phys.* 127 (2007) 114105–114114, <https://doi.org/10.1063/1.2770708>.
- [26] S. Goedecker, M. Teter, J. Hutter, Separable dual-space Gaussian pseudopotentials, *Phys. Rev. B Condens. Mater.* 54 (1996) 1703–1710, <https://doi.org/10.1103/PhysRevB.54.1703>.
- [27] W. Weppner, Oxide semiconductors for solar energy conversion: titanium dioxide, *Int. J. Hydrogen Energ.* 37 (2012) 4535–4537, <https://doi.org/10.1016/j.ijhydene.2011.11.124>.
- [28] O. Yamaguchi, M. Morimi, H. Kawabata, K. Shimizu, Formation and transformation of ZnTiO<sub>3</sub>, *J. Am. Ceram. Soc.* 70 (2010) C-97–C-98, <https://doi.org/10.1111/j.1551-2916.1987.tb05011.x>.
- [29] M.R. Mohammadi, D.J. Fray, Low temperature nanostructured zinc titanate by an aqueous particulate sol-gel route: optimisation of heat treatment condition based on Zn:Ti molar ratio, *J. Eur. Ceram. Soc.* 30 (2010) 947–961, <https://doi.org/10.1016/j.jeurceramsoc.2009.09.031>.
- [30] F.H. Dulln, D.E. Rase, Phase equilibria in the system ZnO-TiO<sub>2</sub>, *J. Am. Ceram. Soc.* 43 (1960) 125–131, <https://doi.org/10.1111/j.1151-2916.1960.tb14326.x>.
- [31] H.L. Cui, W. Zhao, C.Y. Yang, H. Yin, T.Q. Lin, Y.F. Shan, Y. Xie, H. Gu, F.Q. Huang, Black TiO<sub>2</sub> nanotube arrays for high-efficiency photoelectrochemical water-splitting, *J. Mater. Chem. A* 2 (2014) 8612–8616, <https://doi.org/10.1039/C4TA00176A>.
- [32] S.A. Ardizzone, C.L. Bianchi, G. Cappelletti, A. Naldoni, C. Pirola, Photocatalytic degradation of toluene in the gas phase: relationship between surface species and catalyst features, *Environ. Sci. Technol.* 42 (2008) 6671–6676, <https://doi.org/10.1021/es8009327>.
- [33] X.Y. Shen, D.B. Mu, S. Chen, R. Huang, F. Wu, Electrospun composites of ZnO/Cu nanocrystals-implanted carbon fibers as an anode material with high rate capability for lithium ion batteries, *J. Mater. Chem. A* 2 (2014) 4309–4315, <https://doi.org/10.1039/c3ta14685e>.
- [34] O.F. Lopes, K.T.G. Carvalho, A.E. Nogueira, W. Avansi Jr., C. Ribeiro, Controlled synthesis of BiVO<sub>4</sub> photocatalysts: evidence of the role of heterojunctions in their catalytic performance driven by visible-light, *Appl. Catal. B* 188 (2016) 87–97, <https://doi.org/10.1016/j.apcatb.2016.01.065>.
- [35] M.N. Islam, T.B. Ghosh, K.L. Chopra, H.N. Acharya, XPS and X-ray diffraction studies of aluminum-doped zinc oxide transparent conducting films, *Thin Solid Films* 280 (1996) 20–25, [https://doi.org/10.1016/0040-6090\(95\)08239-5](https://doi.org/10.1016/0040-6090(95)08239-5).
- [36] J. Zhang, M.J. Li, Z.C. Feng, J. Chen, C. Li, UV raman spectroscopic study on TiO<sub>2</sub>. I. Phase transformation at the surface and in the bulk, *J. Phys. Chem. B* 110 (2006) 927–935, <https://doi.org/10.1021/jp0552473>.
- [37] J.G. Li, T. Ishigaki, X.D. Sun, Anatase, brookite, and rutile nanocrystals via redox reactions under mild hydrothermal conditions: phase-selective synthesis and physicochemical properties, *J. Phys. Chem. C* 111 (2007) 4969–4976, <https://doi.org/10.1021/jp0673258>.
- [38] L. Li, F.F. Li, T. Cui, Q. Zhou, D.P. Xu, Optical interband transitions in Zn<sub>2</sub>TiO<sub>4</sub> single crystals, *Phys. Status Solidi A* 209 (2012) 2596–2599, <https://doi.org/10.1002/pssa.2012228394>.
- [39] C. Zeng, Y.M. Hu, Y.X. Guo, T.R. Zhang, F. Dong, Y.H. Zhang, H.W. Huang, Facile in-situ self-sacrifice approach to ternary hierarchical architecture Ag/AgX(X=Cl, Br, I)/AgI<sub>0</sub> distinctively promoting visible-light photocatalysis with composition-dependent mechanism, *ACS Sustainable Chem. Eng.* 4 (2016) 3305–3315, <https://doi.org/10.1021/acssuschemeng.6b00348>.
- [40] K.H. Reddy, S. Martha, K.M. Parida, Fabrication of novel p-BiOI/n-ZnTiO<sub>3</sub> heterojunction for degradation of rhodamine 6G under visible light irradiation, *Inorg. Chem.* 52 (2013) 6390–6401, <https://doi.org/10.1021/ic400159m>.
- [41] O.F. Lopes, K.T.G. Carvalho, A.E. Nogueira, W. Avansi Jr., C. Ribeiro, Controlled synthesis of BiVO<sub>4</sub> photocatalysts: evidence of the role of heterojunctions in their catalytic performance driven by visible-light, *Appl. Catal. B* 188 (2016) 87–97, <https://doi.org/10.1016/j.apcatb.2016.01.065>.
- [42] H.T. Yu, X. Quan, S. Chen, H.M. Zhao, Y.B. Zhang, TiO<sub>2</sub>-carbon nanotube heterojunction arrays with a controllable thickness of TiO<sub>2</sub> layer and their first application in photocatalysis, *J. Photochem. Photobiol. A: Chem.* 200 (2008) 301–306, <https://doi.org/10.1016/j.jphotochem.2008.08.007>.
- [43] J. Lim, D. Monllor-Satoca, J.S. Jang, S. Lee, W. Choi, Visible light photocatalysis of fullerol complexed TiO<sub>2</sub> enhanced by Nb doping, *Appl. Catal. B* 152–153, <https://doi.org/10.1016/j.apcatb.2014.01.026> 233–240.
- [44] K. Fan, T.Y. Peng, J.N. Chen, K. Dai, Effects of tetrabutoxytitanium on photoelectrochemical properties of plastic-based TiO<sub>2</sub> film electrodes for flexible dye-sensitized solar cells, *J. Power Sources* 196 (2011) 2939–2944, <https://doi.org/10.1016/j.jpowsour.2010.11.060>.
- [45] Y. Xie, P. Joshi, S.B. Darling, Q.L. Chen, T. Zhang, D. Galipeau, Q.Q. Qiao, Electrolyte effects on electron transport and recombination at ZnO nanorods for dye-sensitized solar cells, *J. Phys. Chem. C* 114 (2010) 17880–17888, <https://doi.org/10.1021/jp106302m>.
- [46] K. Maeda, K. Domen, Photocatalytic water splitting recent progress and future challenges, *J. Phys. Chem. Lett.* 1 (2010) 2655–2661, <https://doi.org/10.1021/jz1007966>.
- [47] K.J. Young, L.A. Martini, R.L. Milot, R.C. Snoeberger III, V.S. Batista, C.A. Schmuttenmaer, R.H. Crabtree, G.W. Brudvig, Light-driven water oxidation for solar fuels, *Coord. Chem. Rev.* 256 (2012) 2503–2520, <https://doi.org/10.1016/j.ccr.2012.03.031>.
- [48] S. Sato, T. Arai, T. Morikawa, Toward solar-driven photocatalytic CO<sub>2</sub> reduction using water as an electron donor, *Inorg. Chem.* 54 (2015) 5105–5113, <https://doi.org/10.1021/ic502766g>.
- [49] V.P. Indrakanti, H.H. Schobert, J.D. Kubicki, Quantum mechanical modeling of CO<sub>2</sub> interactions with irradiated stoichiometric and oxygen-deficient anatase TiO<sub>2</sub> surfaces: implications for the photocatalytic reduction of CO<sub>2</sub>, *Energ. Fuel.* 23 (2009) 5247–5256, <https://doi.org/10.1021/ef9003957>.